ACS OMEGA

http://pubs.acs.org/journal/acsodf

Article

Facile One-Step Pyrolysis of ZnO/Biochar Nanocomposite for Highly Efficient Removal of Methylene Blue Dye from Aqueous Solution

Nguyen Thi Luyen, Khien Van Nguyen, Nguyen Van Dang, Tran Quang Huy, Pham Hoai Linh, Nguyen Thanh Trung, Van-Truong Nguyen, and Dang Van Thanh*

Cite This: *ACS Omega* 2023, 8, 26816−26827

Read Online

ACCESS | Metrics & More | Article Recommendations | Supporting Information

ABSTRACT: In this work, we developed a facile one-step pyrolysis method for preparing porous ZnO/biochar nanocomposites (ZBCs) with a large surface area to enhance the removal efficiency of dye from aqueous solution. Peanut shells were pyrolyzed under oxygen-limited conditions with a molten salt $ZnCl_2$, which played the roles of the activating agent and precursor for the formation of nanoparticles. The effects of the mass ratio between the molten salt $ZnCl_2$ and peanut shells as well as pyrolysis temperature on the formation of ZBCs were investigated. Characterization results revealed that the as-synthesized ZBCs exhibited a highly porous structure with a specific surface area of 832.12 m^2/g, suggesting a good adsorbent for efficient removal of methylene blue (MB). The maximum adsorption capacity of ZBCs on MB was 826.44 mg/g, which surpassed recently reported adsorbents. The formation mechanism of ZnO nanoparticles on the biochar surface was due to $ZnCl_2$ vaporization and reaction with water molecules extracted from the lignocellulosic structures. This study provides a basis for developing a simple and large-scale synthesis method for wastewater with a high adsorption capacity.

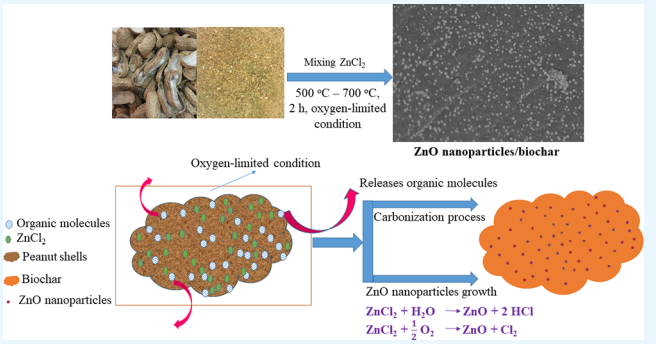

1. INTRODUCTION

Nowadays, the development of industries due to the increasing demands of humans has caused several serious water pollution issues. Inorganic and organic pollution factors, such as heavy metals, toxic dyes, pesticides, etc., are harmful to the human health as well as ecological systems.[1,2] Therefore, many technologies and materials have been developed to solve water pollution issues. Biochar is a traditional adsorbent for treatment of many pollutants due to its high carbon content, nontoxicity, low cost,[3] and environment friendliness and thus has a high wastewater treatment potential.[4−6] For instance, cattle manure-derived biochar was employed as an adsorbent for the removal of methylene blue (MB) from aqueous solutions.[7] Coconut husk-derived biochar was also applied for the remediation of ciprofloxacin and tetracycline in wastewater.[8]

A combination of biochar and nanomaterials has been developed to improve adsorption capacity through several mechanisms, such as enhancing the porous structure and increasing the number of surface functional groups and the surface-to-volume ratio.[9−11] Techniques used to combine biochar and nanomaterials include impregnation,[12−15] chemical coprecipitation,[13,16] direct pyrolysis,[17−19] and others.[20,21] The porous carbon structure can be improved by activating the raw material with agents, such as $ZnCl_2$, $FeCl_3$, KOH, and H_3PO_4, in two different ways: aqueous state and solid state. ZnO nanoparticles are then loaded onto the biochar surface through self-reduction or precipitation mild pyrolysis. However, the long processing time and difficulty in the formation of ZnO phase porous nanocomposite have hindered their practical applications. A facile and efficient method for preparing ZnO/biochar nanocomposites should be developed.

$ZnCl_2$, a molten salt, is widely used to convert biomass to porous carbon in an inert environment through carbonization at 450 °C.[22] Given its low-melting-point temperature, $ZnCl_2$ could promote dehydration reactions in the carbon precursor, eliminate the formation of tars, and accelerate charring and aromatization, thus boosting carbon-based yields. At mild and high temperatures, $ZnCl_2$ creates more micro/macropores through melting and templating.[23−25] Studies have typically implemented the direct pyrolysis of $ZnCl_2$ and raw materials in the inert atmosphere to produce porous carbon materials with $ZnCl_2$ as the activating agent. For example, Wang et al.[26] activated $ZnCl_2$ and walnut shell by microwave-assisted pyrolysis. Dos Reis et al.[27] activated $ZnCl_2$ and sludge by

Received: February 25, 2023
Accepted: July 13, 2023
Published: July 24, 2023

conditional or microwave-assisted pyrolysis. Shang et al.[22] activated $ZnCl_2$ and peanut shells by conditional pyrolysis. Wang et al.[28] activated $ZnCl_2$ and sewage sludge through microwave irradiation. ZnO/biochar was prepared using a two-step method by impregnation/chemical coprecipitation of biochar in zinc-containing salt or impregnation of biochar with ZnO nanoparticles in acid/basic media.[21,29−31] ZnO nanoparticles were then loaded on the biochar surface through self-reduction. $ZnCl_2$ has been successfully used as an activating agent in the synthesis of porous carbon materials. However, studies have not discussed the role of $ZnCl_2$ in the formation of ZnO nanoparticles through simple one-step pyrolysis synthesis of ZnO/biochar nanocomposite under oxygen-limited conditions.

In this work, we adopted a facile and one-step pyrolysis method for preparing porous ZnO/biochar nanocomposites from agricultural wastes of peanut shells and molten $ZnCl_2$ under oxygen-limited condition. For the first time, we explored the formation mechanism of ZnO nanoparticles on the biochar surface. This method is cost-effective, uses abundant available raw materials, and is simple and easy to scale up.

2. MATERIALS AND METHODS

2.1. Materials. Peanut shells were collected from a local market in Thai Nguyen province, Vietnam. Zinc chloride ($ZnCl_2 \geq 98\%$) and silver nitrate ($AgNO_3$, 98%) were obtained from Sigma-Aldrich. Methylene blue was purchased from Xilong, China. All chemicals were directly used without further purification.

2.2. One-Step Synthesis of ZnO/Biochar Nanocomposites. ZnO/biochar nanocomposites were synthesized by a facile one-step pyrolysis method under oxygen-limited condition based on the direct physical mixture of molten salt $ZnCl_2$ and peanut shells. The peanut shells were first washed to remove adhering dirt on the surface, dried at 100 °C for 24 h, ground, and passed through a sieve with a pore size of 0.154 mm. The molten salt $ZnCl_2$ and peanut shells were physically mixed by hand at various mass ratios of 0.2, 1, 2, 3, and 4 wt.

Pyrolysis was carried out in a muffle furnace (Smart XMT-900) with the heating rate of 10 °C.min^{-1} under oxygen-limited condition. The prepared mixture was placed in a porcelain cup with a lid without inert gas fluxed during pyrolysis at 400, 500, 600, and 700 °C for 2 h. The furnace was then cooled down to room temperature to obtain ZBCs. The samples were washed several times with DI water and added with few drops of $AgNO_3$ solution (0.1 M) until no Cl^- ions existed. The samples were dried at 60 °C for 24 h and named as ZBC with the corresponding mass ratio as the suffix. For example, ZBCs pyrolyzed at 500 °C with the mass ratio of $ZnCl_2$ and peanut shells set as 0.2, 1, 2, 3, and 4 wt were named ZBC-0.2, ZBC-1; ZBC-2, ZBC-3, and ZBC-4, respectively. The ZBCs were denoted as ZBC-400, ZBC-500, ZBC-600, and ZBC-700 when the mass ratio of $ZnCl_2$ and peanut shells was fixed at 3 wt and the activation temperature was changed to 400, 500, 600, and 700 °C. The biochar pyrolyzed at 500 °C inactivated $ZnCl_2$ (denoted as BC).

2.3. Characterization. The morphological and elemental composition of the materials was characterized by field emission scanning electron microscopy (FE-SEM; Hitachi-S4800) and transmission electron microscopy (TEM; JEM 1400 flash). Specific surface area was analyzed on a surface area analyzer (TriStar 3000 V6.07 A) using N_2 adsorption/desorption isotherms at 77 K. The pore size distribution and total pore volume of the samples were estimated through the Barrett−Joyner−Halenda (BJH) method. X-Ray diffraction (XRD) patterns were recorded using an X-ray diffractometer (Bruker D2). The surface chemical functional groups of the samples were characterized by Fourier transform infrared spectroscopy (FTIR-4600 Jasco in the region of 400−4000 cm^{-1}). Raman spectra (RS) were recorded using an Xplora Plus (Horiba) microscope.

2.4. Adsorption Experiments. A 1000 mg/L MB solution was prepared by dissolving MB in DI water and named as stock solution. MB solutions with different concentrations ranging from 50 to 500 mg/L were diluted from the stock solution. All adsorption experiments were performed in batch mode. In brief, 25 mg of adsorbent material was mixed with 25 mL of MB solution in a 100 mL flask and shaken at 200 rpm for specific time at room temperature. The effects of mass ratio and pyrolysis temperature on the adsorption capacity of ZnO/biochar nanocomposite were determined in a series of experiments with an initial MB concentration of 200 mg/L and a pH of 7.0. ZBCs were shaken in MB solutions with different initial concentrations ranging from 50 to 500 mg/L for 120 min at pH 7.0 to identify the adsorption isotherm. After each adsorption experiment, the adsorbents were separated by centrifugation at 6000 rpm for 5 min. The concentrations of MB were determined by measuring the absorbance of the solution at the wavelength of 664 nm by an ultraviolet−visible (UV−Vis) spectrophotometer (Jasco V-770) at room temperature. Similarly, adsorption experiments with methylene orange (MO) and methylene violet (MV) are conducted for comparison.

Removal efficiency (%) and adsorption capacity (mg/g) were calculated using the following equations:

$$E = \frac{C_0 - C_e}{C_0} 100 \tag{1}$$

$$q_e = \frac{(C_0 - C_e)V}{M} \tag{2}$$

where q_e (mg/g) is the amount of MB adsorbed on the adsorbent at equilibrium; C_0 and C_e (mg/L) are the initial MB concentration and MB concentration at equilibrium, respectively; V (L) is the volume of the solution; and M (g) is the mass of the adsorbent.

Three isotherm models such as Langmuir, Freundlich, and Temkin were considered. The equations of the models were as follows:

Langmuir isotherm:

$$\frac{C_e}{q_e} = \frac{C_e}{q_{max}} + \frac{1}{K_L q_{max}} \tag{3}$$

Freundlich isotherm:

$$\ln q_e = \ln K_F + \frac{1}{n} \ln C_e \tag{4}$$

Temkin isotherm:

$$q_e = B \ln K_T + B \ln C_e \tag{5}$$

where C_e is the MB concentration at equilibrium (mg/L), q_e is the adsorption capacity at equilibrium (mg/g), q_{max} is the maximum adsorption capacity (mg/g), K_L is the Langmuir constant (L/mg), K_F is the Freundlich constant [(mg/g) (L/

https://doi.org/10.1021/acsomega.3c01232
ACS Omega 2023, 8, 26816−26827

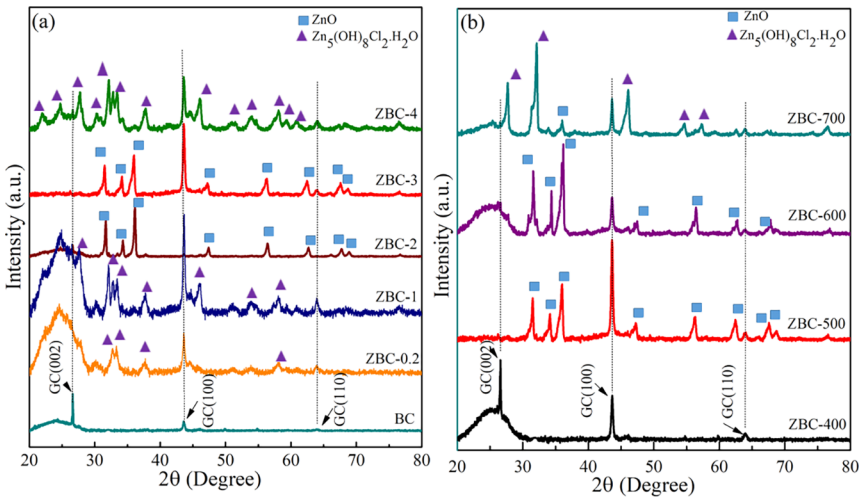

Figure 1. XRD patterns of samples obtained at different (a) mass ratios of $ZnCl_2$ and peanut shells; and (b) pyrolysis temperatures. The crystal structure of graphitic carbon is labeled GC.

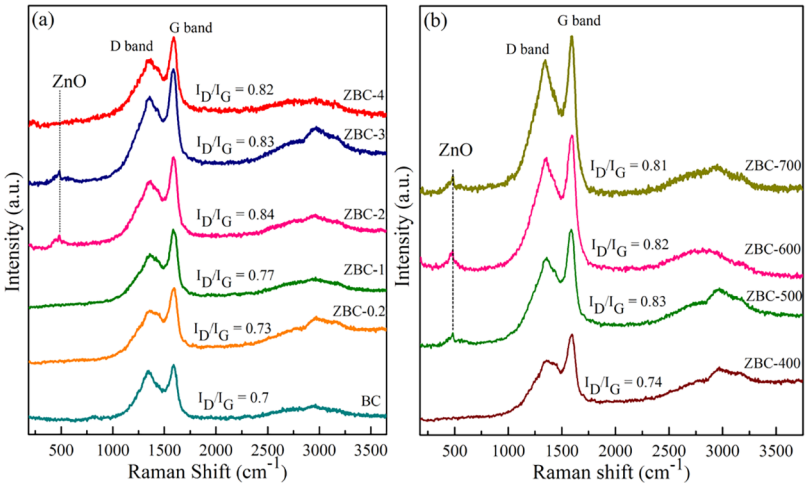

Figure 2. Raman spectra of samples obtained at different (a) mass ratios of $ZnCl_2$ and peanut shells and (b) pyrolysis temperatures.

mg)$^{1/n}$], K_T is the equilibrium constant (L/g), and B is related to the heat of adsorption.

Three kinetic models were used to analyze the adsorption data and expressed in eqs 6−8:

The pseudo-first order model:

$$q_t = q_e\,(1 - e^{k_1 \cdot t}) \tag{6}$$

The pseudo-second order model:

$$\frac{t}{q_e} = \frac{1}{k_2 \cdot q_e^2} + \frac{1}{q_e} t \tag{7}$$

The Weber-Morris model:

$$q_t = k_w \cdot t^{1/2} + I \tag{8}$$

where k_1 is the rate constant for first-order adsorption (g. mg^{-1}.min^{-1}), k_2 is the rate constant for second-order adsorption (g. mg^{-1}.min^{-1}), k_w is the intraparticle rate constant, $t^{1/2}$ is the square root of time, I is the intercept, q_e is the adsorption capacity at equilibrium (mg/g), and q_t is the adsorption capacity at any time t (mg/g).

3. RESULTS AND DISCUSSION

3.1. Structural Characterization. XRD was used to determine crystallized structures and the formation of ZnO nanoparticles on the biochar surface. Figure 1a,b represents the XRD patterns corresponding to the samples against different mass ratios of $ZnCl_2$ and peanut shells and pyrolysis temperatures. As shown in Figure 1a, the XRD pattern for peanut shells inactivated by $ZnCl_2$ (BC sample) had characteristic peaks at 2θ of 26.62°, 43.59°, and 63.94°, which are indexed to the (002), (100), and (110) planes, respectively. The (002), (100), and (110) reflections could be attributed to the honeycomb lattice in hexagonal graphitic carbon and monolayer graphitic carbon, respectively, consistent with previous studies.[32−34] For ZBC-2 and ZBC-3 samples (Figure 1a), the characteristic peaks of ZnO crystalline at 2θ of 31.48°, 34.18°, 35.97°, 47.35°, 56.26°, 62.45°, 67.64°, and 68.78° correspond to the planes of (100), (002), (101), (102), (110), (103), (112), and (201), respectively, as verified with JCPDS 36-1451 for the wurtzite of ZnO.[35] Additionally, increasing $ZnCl_2$ (ZBC-3 sample) caused ZnO nanoparticles to be smaller in size than ZBC-2. For ZBC-0.2, ZBC-1, and ZBC-4, the appearance of $Zn_5(OH)_8Cl_2.H_2O$ or simonkolleite compound (JCPDS 07-0155) was observed instead of the

https://doi.org/10.1021/acsomega.3c01232
ACS Omega 2023, 8, 26816−26827

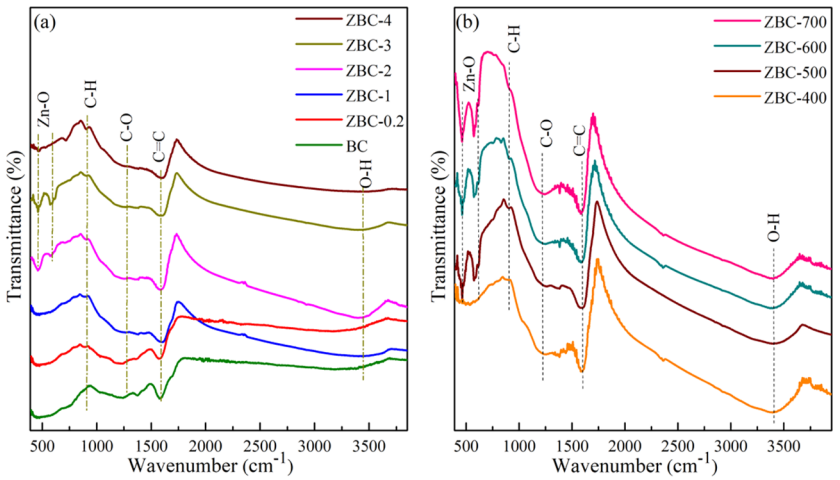

Figure 3. FTIR spectra of samples obtained at different (a) mass ratios of $ZnCl_2$ and peanut shells and (b) pyrolysis temperatures.

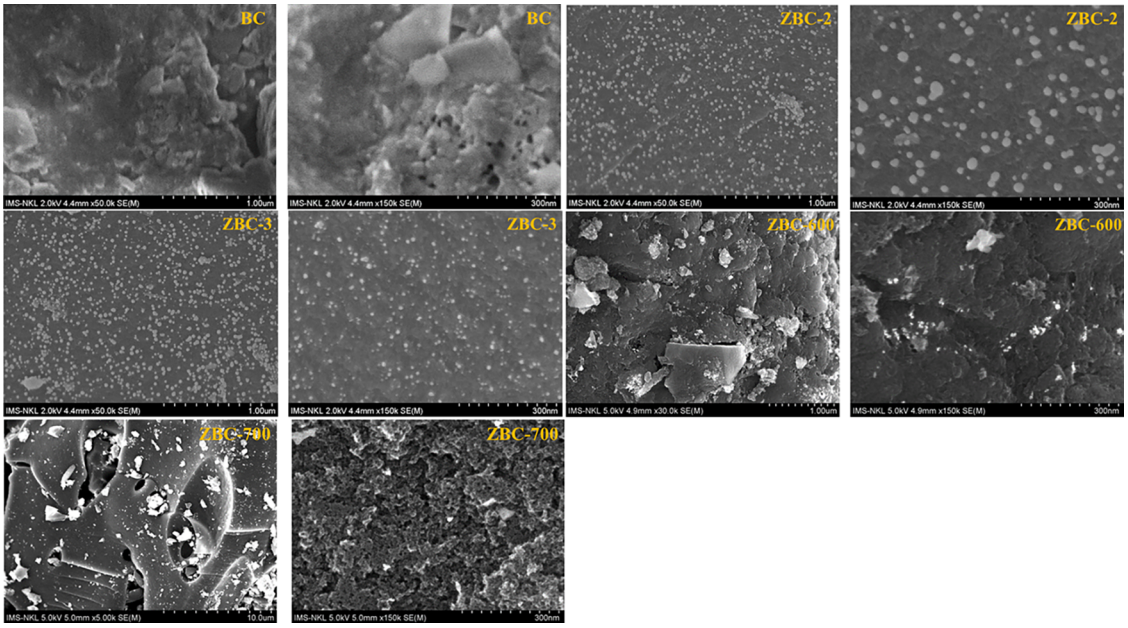

Figure 4. FE-SEM images of BC, ZBC-2, ZBC-3, ZBC-600, and ZBC-700.

characteristic peaks of ZnO nanoparticles. This finding indicated that the lower or higher content of molten $ZnCl_2$ prevented the formation of ZnO nanoparticles[36] and subsequently formed simonkolleite layered-platelet structures.[37]

As displayed in Figure 1b, ZBC-400 exhibited all characteristic peaks belonging to biochar. This result suggested that the temperature of 400 °C was not sufficiently high to evaporate molten $ZnCl_2$; therefore, ZnO nanoparticles were not formed on the biochar surface. Previous studies[22,36] showed that molten $ZnCl_2$ evaporated at 480 °C. When the pyrolysis temperature was increased to 500 and 600 °C, typical peaks of ZnO nanoparticles were found on the biochar surface (ZBC-500 and ZBC-600 samples). At the pyrolysis temperature of 700 °C, a transformation phase to former $Zn_5(OH)_8Cl_2.H_2O$ structure was detected. With increasing temperature from 500 to 600 °C, molten $ZnCl_2$ evaporated, decomposed organic molecules, and promoted the water molecule extraction from the lignocellulosic structures of the raw material to form ZnO nanoparticles on the biochar surface. Hence, the evaporation of molten $ZnCl_2$ and the decomposition of organic molecules to form ZnO nanoparticles on the biochar surface occurred under the suitable mass ratio of $ZnCl_2$ and peanut shells (2 and 3 wt) at the pyrolysis temperature of 500−600 °C.

Raman spectroscopy is used to investigate variations in the structure of samples.[38] Similar to the XRD analysis, the Raman study proved the presence of the layered graphite-like structure and the formation of ZnO nanoparticles on the biochar surface. Figure 2 shows the Raman spectra of the samples against different mass ratios of $ZnCl_2$ and peanut shells and pyrolysis temperatures.

Two characteristic bands were detected, namely, D band at 1354 cm^{-1} and G band at 1594 cm^{-1}. The D band is related to the disordered/defect in the carbonaceous structure, while the G band is assigned to the ordered graphitic structure.[36,39,40] The peak intensity ratio (I_D/I_G) represents the disordered degree of carbon. The I_D/I_G values of ZBC-2, ZBC-3, ZBC-500, ZB-600, and ZBC-700 (I_D/I_G = 0.81−0.84) fitted by Gauss and Lorentz function are notably higher than that of the remaining samples (I_D/I_G = 0.7−0.77). This finding indicated

https://doi.org/10.1021/acsomega.3c01232
ACS Omega 2023, 8, 26816−26827

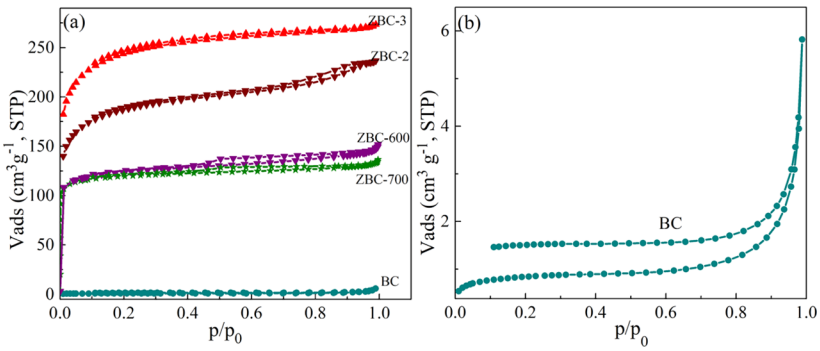

Figure 5. (a) N_2 isotherms at −196 °C for the ZBCs, and biochar; (b) magnified view of biochar.

the significant improvement in the defect structure of biochar by using $ZnCl_2$ chemical activation.[34] Furthermore, the vibrational modes of Zn-O at about 484 cm^{-1} were found for ZBC-2 and ZBC-3 (Figure 2a) as well as ZBC-500, ZBC-600, and ZBC-700 (Figure 2b). This finding proved the presence of ZnO nanoparticles on the biochar surface, while other studies reported that the vibrational mode of ZnO nanoparticles cannot be observed on Raman spectra.[17,41,42]

The presence of functional groups would help determine the formation of ZnO nanoparticles on the biochar surface. Figure 3 displays the FTIR spectra of the samples against different mass ratios of $ZnCl_2$ and peanut shells and pyrolysis temperatures.

For all the samples, the peaks located at 3424 and 1578 cm^{-1} are assigned to the stretching vibration of O−H and C═C, respectively. The peak located at 1221 cm^{-1} could be attributed to the stretching vibration of C−O, whereas the peak observed at 889 cm^{-1} could be due to the stretching vibration of the C−H bond.[43,44] For ZBC-2 and ZBC-3 (Figure 3a) as well as ZBC-500, ZBC-600, and ZBC-700 samples (Figure 3b), the peaks centered at 461 and 581 cm^{-1} could be attributed to the Zn−O stretching vibration,[45] respectively, indicating the formation of ZnO nanoparticles on the biochar surface.

3.2. Morphology of Materials. Figure 4 shows the FE-SEM images of peanut shells inactivated by molten salt $ZnCl_2$ (BC) and peanut shells activated by molten salt $ZnCl_2$ (ZBCs) at different factors of magnification. When the peanut shells were inactivated by molten salt $ZnCl_2$, the BC sample had a rough surface with 26.5 nm wide pore structures. In the ZBCs obtained at the mass ratio of $ZnCl_2$ and peanut shells of 2 and 3 (ZBC-2 and ZBC-3), ZnO nanoparticles were formed on the biochar surface. This finding was also observed on the EDX spectrum in Figure S1 and Table S1. The diameter of ZnO particles in ZBC-3 is about 10−20 nm smaller than those in ZBC-2, consistent with the XRD pattern. ZBC-600 also showed the formation of ZnO nanoparticles on the biochar surface, but the observed grain boundaries were not clear. The number of ZnO particles on the biochar surface is lower than those in ZBC-700, indicating the formation of pores, and some of which may be occupied or blocked by ZnO nanoparticles formed. For the first time, our results revealed that molten salt $ZnCl_2$ not only acted as an activating agent but also as a precursor that promoted the growth of ZnO nanoparticles on the biochar surface under oxygen-limited conditions.

3.3. Textural Characteristics. The N_2 adsorption−desorption isotherms at −196 °C of ZBCs and BC samples are displayed in Figure 5a,b. According to IUPAC classification, the nitrogen adsorption−desorption isotherms of ZBCs and BC can be classified as a mixture of types I and IV. The isotherms of ZBCs are primarily microporous, with a significant contribution from mesoporous pores. Increasing the mass ratio of $ZnCl_2$ and peanut shells resulted in a larger surface area in the range of 2−3. This finding is consistent with the behavior of other activating agents, such as H_3PO_4 and KOH, where high impregnation ratios typically result in activated carbons with a higher contribution of mesoporosity. The sample with peanut shells inactivated by molten salt $ZnCl_2$ (BC sample) had negligible nitrogen adsorption and low BET surface area (only 2.9 m^2/g) and porosity (Figures 5 and 6b and Table 1). The absence of significant porosity is confirmed by the SEM images of the BC sample.

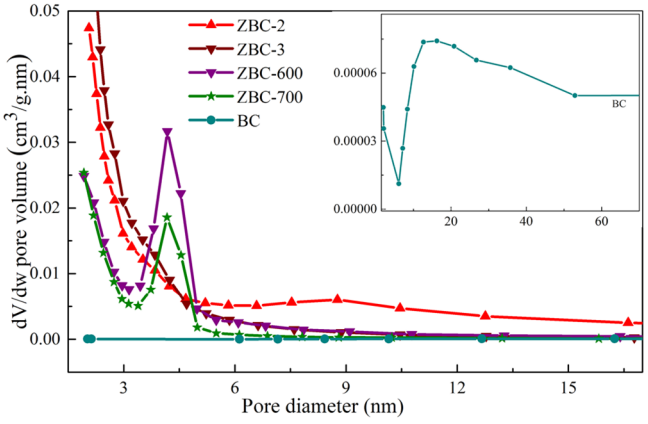

Figure 6. Pore size distribution curves of the biochar, and ZBCs.

The highest BET surface area obtained at 500 °C with the mass ratio of $ZnCl_2$ and peanut shells of 3 was 832.1 m^2/g (Table 1). This finding could be explained by the formation of small ZnO nanoparticles on the biochar surface and within the porous structure of the ZBCs. These particles could block the

Table 1. Characteristic Parameters of the Porous Structure of the Materials

sample	S_{BET} (m^2 g^{-1})	S_t (m^2 g^{-1})	V_{micro} (cm^3 g^{-1})	pore size (nm)	S_t/S_{BET}
BC	2.9	0.46	0.001	33.73	0.160
ZBC-2	639.8	85.95	0.256	4.77	0.134
ZBC-3	832.1	87.11	0.344	3.23	0.105
ZBC-600	525.4	54.37	0.229	4.28	0.103
ZBC-700	492.2	36.99	0.207	3.64	0.075

https://doi.org/10.1021/acsomega.3c01232
ACS Omega 2023, 8, 26816−26827

Scheme 1. Illustration of the Formation of ZnO/Biochar Nanocomposites

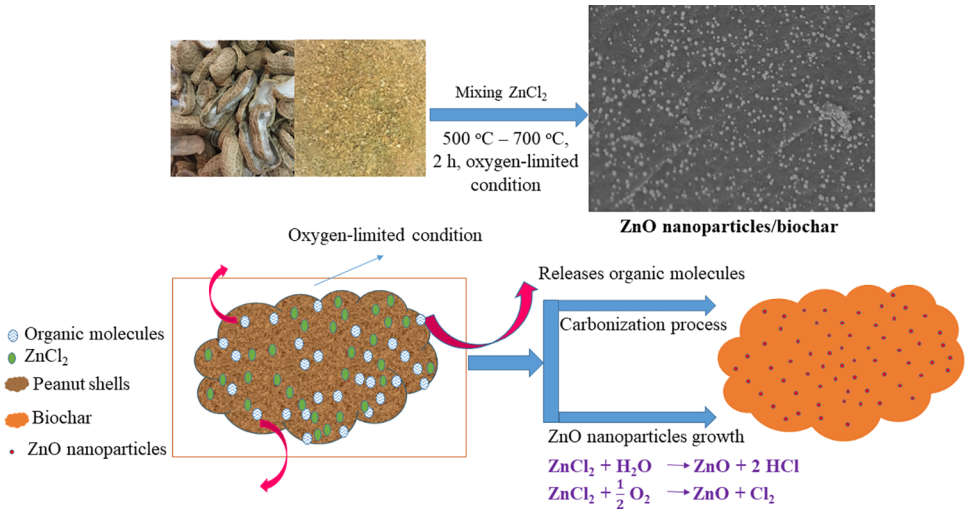

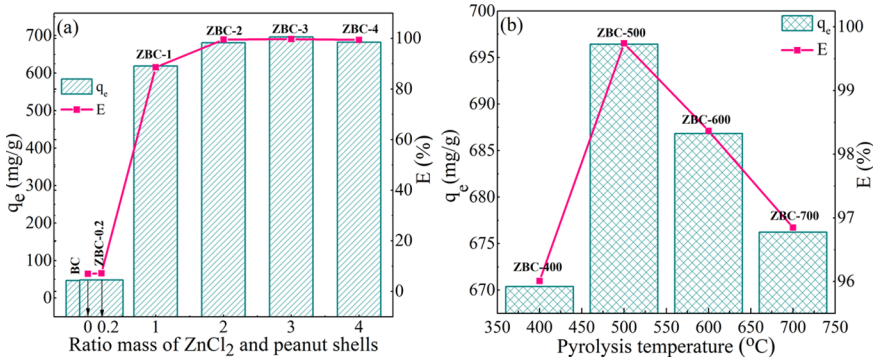

Figure 7. Removal efficiency and adsorption capacity of (a) samples synthesized at different (a) mass ratios of $ZnCl_2$ and peanut shells and (b) pyrolysis temperatures.

pores and decrease the amount of nitrogen adsorbed, BET surface area, and porosity.[43]

The obtained surface area is in good agreement with previous studies that used related techniques by $ZnCl_2$ activation of carbon precursors. Wang et al.[28] achieved 377.1 m^2/g from sewage sludge and $ZnCl_2$ solution with a mass ratio of 1:2. Dos Reis et al.[27] identified the optimum parameters including the pyrolysis temperature of 500 °C, an activation time of 15 min, a ratio of $ZnCl_2$: a sludge of 0.5, and S_{BET} values of 679 m^2/g. Arami-Niya et al.[46] obtained the S_{BET} range of 727.91−1118 m^2/g by using $ZnCl_2$ solution as the activating agent and the oil palm shell as the precursor at a mass ratio of 0.53 at different physical activation times of 1−7 h. Xia et al.[23] tested two different chemical activators, namely, $ZnCl_2$ and NaOH, as activating agents of pig manure slurry. The highest surface area (517.67 m^2/g) was obtained with $ZnCl_2$ through solution impregnation. The micropore volume increased with temperature, reaching a maximum of 0.344 cm^3/g for ZBCs obtained at 500 °C (ZBC-3); when the pyrolysis temperature was increased to 700 °C, the value decreased to 0.207 cm^3/g possibly due to the collapse of adjacent pore walls. This finding could explain why the pore size is larger at higher pyrolysis temperatures (Table 1), similar to the results obtained at the same temperature range in the study of Rodríguez-Sánchez et al.[43]

The porous structure results explained why biochar had lower MB adsorption capacity than ZnO/biochar nanocomposites, which will be discussed in the following section. Previous studies also showed the relationship between adsorption capacity and pore diameter/BET surface area.[47,48]

The characteristic parameters of the porous structure of the materials are shown in Table 1.

3.4. Formation Mechanisms of ZnO/Biochar Nanocomposites. Based on the results of XRD, RS, FTIR, and FE-SEM analyses, we illustrated the formation of ZnO nanoparticles on the biochar surface in Scheme 1.

First, carbonization was used to convert peanut shells into a porous carbon material due to the molten-salt $ZnCl_2$ process. Second, in the range of suitable pyrolysis temperatures and mass ratios of $ZnCl_2$ and peanut shells, the evaporation of $ZnCl_2$ started and released organic molecules, such as hemicellulose, cellulose, and lignin to form the porous structure of biochar.[49] The formation of ZnO nanoparticles could be due to $ZnCl_2$ vaporization, and their reaction with water molecules extracted from the lignocellulosic structures of the carbon precursors at a high temperature according to the following reaction:

$$ZnCl_2 + H_2O \rightarrow ZnO + 2HCl \quad (9)$$

The reaction was carried out under oxygen-limited conditions, where little O_2 contents were present; subsequently, $ZnCl_2$ could be partly oxidized into ZnO nanoparticles by the following equations:[50]

https://doi.org/10.1021/acsomega.3c01232
ACS Omega 2023, 8, 26816−26827

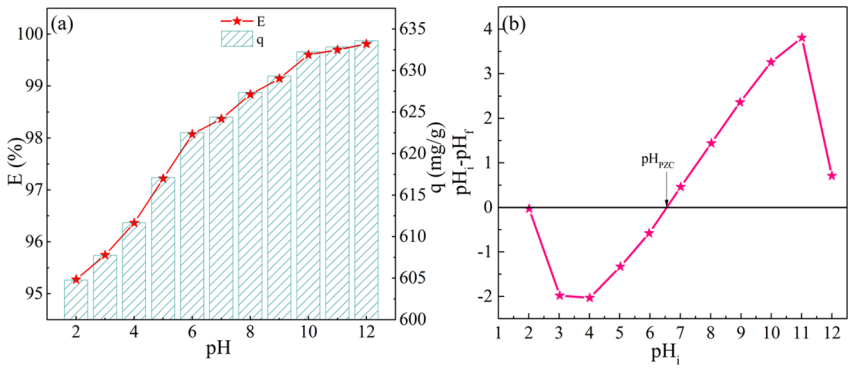

Figure 8. (a) Effect of pH on MB adsorption at an initial concentration of 200 mg/L, an adsorbent dose of 25 mg ZBC-3/25 mL solution, a contact time of 120 min, a temperature of 30 °C, and (b) pH_{PZC} of ZBC-3.

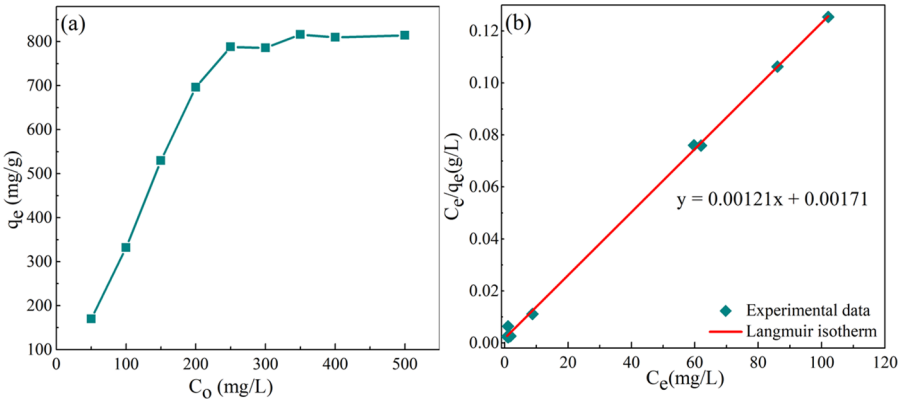

Figure 9. (a) Effect of initial concentrations on MB adsorption by ZnO/biochar; (b) experimental data fitted with the Langmuir model.

$$ZnCl_2 + 1/2O_2 \rightarrow ZnO + Cl_2 \quad (10)$$

3.5. Adsorption Properties. The removal efficiency and adsorption capacity of various adsorbent materials synthesized at different mass ratios and pyrolysis temperatures were investigated. All experiments were conducted at a contact time of 120 min, an adsorbent dose of 25 mg/25 mL, and an initial MB concentration of 200 mg/L. Figure 7a displays the effect of different mass ratios to the removal efficiency and adsorption capacity of MB.

As shown in Figure 7a, the adsorbents inactivated and activated by molten $ZnCl_2$ with the mass ratio of 0.2 wt had removal efficiencies of only 6.95 and 7.19% for MB; the adsorption capacities were 46.68 and 48.31 mg/g, respectively. When increasing mass ratio from 1 to 4 wt, the removal efficiency and adsorption capacity of MB increased quickly and reached the maximum values of 99.74% and 696.43 mg g^{-1}, respectively, when the ratio mass by 3 wt. Hence, increasing the mass of $ZnCl_2$ might provide a sufficient melting liquid phase and embed biomass completely,[22] leading to the enhanced adsorption capacity of MB. Table 1 shows that the surface area and average pore diameter of ZnO/biochar nanocomposites activated by molten $ZnCl_2$ were larger than those of biochar inactivated by molten $ZnCl_2$. Based on the BET analysis, ZnO/biochar nanocomposites could provide more adsorption sites, promoting contact between the adsorption sites and MB molecules and increasing the adsorption capacity of MB in comparison to BC. In contrast, the adsorption capacity for MB was mitigated with the increase in the mass ratio of $ZnCl_2$ and peanut shells of 4 wt. Excessive $ZnCl_2$ during activation resulted in pore expansion and reduced adsorption capacity.[18] Figure 7b shows the removal efficiency and adsorption capacity of samples prepared at different pyrolysis temperatures on the adsorption of MB. The highest removal efficiency and adsorption capacity were achieved at 500 °C. As predicted, the adsorption capacity was related to the porosity of adsorbents, which was highly dependent on pyrolysis temperature, the mass ratio of activating agent and peanut shells, activation time, or types of carbonaceous precursors. Indeed, increasing the pyrolysis temperature produced adsorbents with more porosity; however, using a very high pyrolysis temperature may lead to lower porosity due to structural deformation. Increasing the temperature above 500 °C reduced the adsorption performance. Among the as-prepared samples, ZBC-3 was selected to study adsorption isotherms and kinetics because of its high adsorption capacity.

3.6. Effect of Initial pH on the Adsorption Properties of ZnO/Biochar toward MB Dye. The pH of the dye solution influences the adsorption capacity because it influences the degree of ionization of the dye and the surface properties of the adsorbent. Figure 8 shows the effect of pH on the adsorption capacity of MB and the efficiency of ZnO/biochar materials. When the pH of the solution was increased from 2 to 9, the amount of MB adsorbed onto ZnO/biochar and the MB removal efficiency increased significantly. In the solution with pH 9, the adsorption capacity and MB removal efficiency were 629.32 mg g^{-1} and 99.14%, respectively. When the pH was between 10 and 12, the adsorption capacity and MB removal efficiency became stable, reaching 663.57 mg g^{-1} and 99.81%, respectively.

https://doi.org/10.1021/acsomega.3c01232
ACS Omega 2023, 8, 26816−26827

These results indicated that when $pH_{solution} > pH_{PZC}$ (the pH_{PZC} value of 6.54 for ZnO/biochar), the OH^- ions had negative charge. The electrostatic interaction between the cationic MB and OH^- ions increased, thereby increasing the MB adsorption. At $pH_{solution} < pH_{PZC}$, the surface of ZnO/biochar became positively charged, and the competition from H^+ and positively charged MB cations reduced MB adsorption.

3.7. Adsorption Isotherms. Adsorption isotherms are used to assess adsorption or potential interactions between solution and insoluble phases. The effect of initial MB concentration on the adsorption of MB onto ZnO/biochar was investigated by adding 0.025 g of ZBC-3 to 25 mL of various initial MB concentrations (50, 100, 150, 200, 250, 300, 350, 400, and 500 mg/L) at room temperature (Figure 9a). As the initial MB concentration increased, the adsorption capacity of ZnO/biochar increased. When the initial MB concentration was increased from 50 to 500 mg/L, the adsorption capacity increased significantly from 170.01 to 814.28 mg g^{-1}. The higher initial MB concentration offers a stronger driving force due to a larger concentration gradient between MB in the solution and MB on the adsorbent surface.

The theories of Langmuir, Freundlich, and Temkin were employed to examine the isotherm behavior of MB adsorption onto ZnO/biochar (eqs 3−5). The corresponding parameters for the adsorption isotherms are shown in Figure S2 and Table S2. The adsorption data were well fitted with the Langmuir model due to its high correlation coefficient (R^2) of 0.999 (Figure 9b).

This finding indicated the homogeneous adsorption of MB onto the surface monolayer of the ZnO/biochar, implying that the adsorbents have a homogeneous adsorption surface and that all the adsorption sites have the same adsorbate affinity. From the slope and intercept, the values of q_{max} and K_L were estimated to be 826.44 mg g^{-1} and 0.7077 L/mg, respectively. The E_a (activation energy) calculated was 0.86 kJ/mol, indicating that the adsorption of MB on ZnO/biochar was a chemical process.[48] The R_L values of 0.0015−0.0081 from the Langmuir isotherm indicated that the nature of adsorption of MB on the ZnO/biochar was favorable ($0 < R_L < 1$). Compared with previously reported MB adsorption capacities (Table 2), the adsorption capacity of ZnO/biochar for MB (826.44 mg/g) was higher and became almost 100% higher than the highest previously reported adsorption capacity (476.19 mg/L).[51] Additionally, adsorption experiments with methylene orange (MO) and methylene violet (MV) are also conducted for comparison (see details in S4−S7, Supporting Information). The obtained results ZnO/biochar is extremely efficient in adsorbing MB as well MO and MV.

3.8. Adsorption Kinetics. Adsorption kinetics is necessary to understand the adsorption mechanism of ZnO/biochar. In this study, MB adsorption on ZnO/biochar as a function of contact time was investigated using initial MB concentration of 200 mg/L (Figure 10a). The amount of adsorbed MB increased with increasing contact time. The MB adsorption on ZnO/biochar began with rapid adsorption in the first 60 min, followed by slow adsorption that gradually reached equilibrium. The adsorption equilibrium was reached in 120 min, and the ZnO/biochar equilibrium adsorption capacity was 693.1 mg g^{-1}. The rapid adsorption of MB in the early stages could be attributed to increased availability of the uncovered surface and active sites on the adsorbent surface. The rate of adsorption decreased as these absorbing sites became gradually occupied. The adsorption kinetics data were analyzed using pseudo-first order, pseudo-second order, and Weber−Morris models (eqs 6−8, respectively). The kinetics parameters for MB adsorption onto ZnO/biochar nanocomposites are shown in Figure S3 and Table S3. Among the three models, the pseudo-second order model describes the data best based on the nonlinear regression coefficient (R^2). The correlation coefficient (R^2) values for the pseudo-first order and pseudo-second order models were 0.992 and 0.999, respectively. However, the equilibrium rate constant of the pseudo-first order adsorption had a negative value, and the pseudo-first-order model could not be used to describe the adsorption kinetics. The q_{max} value estimated by the pseudo-second-order kinetics model ($q_{e,cal}$ in Table S3) was 694.44 mg g^{-1}, which agrees well with the experimentally determined value ($q_{e,exp}$ in Table S3) of 682.32 mg g^{-1}. Hence, the pseudo-second order kinetic equation better fitted the adsorption process of MB on ZnO/biochar (Figure 10b). The adsorption process of ZnO/biochar and MB was determined by chemical adsorption.

Table 2. Adsorption Capacities of Reported Adsorbents for Methylene Blue

adsorbent	optical pH	initial concentration of dyes (mg/L)	q_e (mg/g)	reference
magnetic activated carbon	not publish	[MB] = 50−500	228.22	48
	2.78	[MO] = 1.0−40	144.93	52
	8.0	[MV] = 25−100	105.26	53
activated carbon	10	[MB] = 40−100	217.35	54
	3	[MO] = 40−100	105.2	
	10	[MV] = 40−100	320.5	
graphene oxide	6.0	[MB] = 40−120	243.90	55
	not publish	[MO] = 10−60	63.84	56
	2.5	[MV] = 10−50	2.47	57
carbon nanotubes	7.0	[MB] = 200−270	399	58
	7.0	[MO] = 80−120	149	58
	6.0	[MV] = 25−150	90.52	59
nanosheet MFI zeolite	10	[MB] = 10−250	476.19	51
	1.0	[MO] = 10−50	4.71	60
	7.5	[MV] = 0−300	141.8	61
MgAl-LDH/biochar	12	[MB] = 5−500	406.47	62
	7	[MO] = 1−12	21.8	63
	6	[MV] = 50−500	374.68	64
ZnO/biochar	6.1	[MB] = 50−500	826.44	this study
	6.0	[MO] = 50−500	301.48	
	6.0	[MV] = 50−500	383.63	

3.9. Possible Adsorption Mechanisms. The TEM images and FTIR spectra of the prepared ZnO/biochar before and after MB adsorption are shown in Figure 11. Figure 11a,b shows the TEM images of ZBC-3 before MB adsorption. ZnO nanoparticles were formed on the biochar surface (Figure 11a, magnification 104,000×). As shown in Figure 11b (magnification 80,000×), pores with diameters of 2−5 nm are loaded on the surface of ZnO/biochar. After MB adsorption, pores and the layer-like porous structure of ZnO/biochar were almost filled (Figure 11c, magnification 40,000×; Figure 11d, magnification 100,000×). The ZnO nanoparticles were partially embedded in the interior or surface of a hole (Figure 11d).

Based on the functional groups of ZnO/biochar in Figure 2, the ZnO/biochar surface has some oxygen-containing functional groups, as confirmed by the presence of the character-

https://doi.org/10.1021/acsomega.3c01232
ACS Omega 2023, 8, 26816−26827

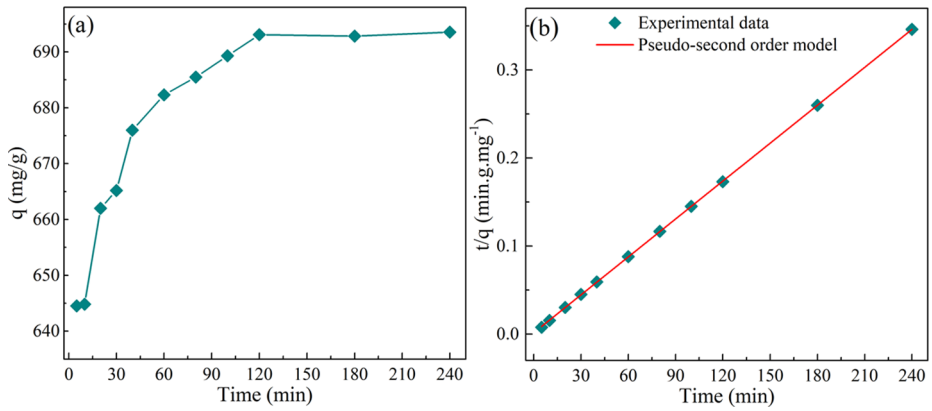

Figure 10. (a) Effect of contact time on MB adsorption onto ZnO/biochar at initial MB concentration of 200 mg/L; (b) the fitted results according to the pseudo-second order kinetics.

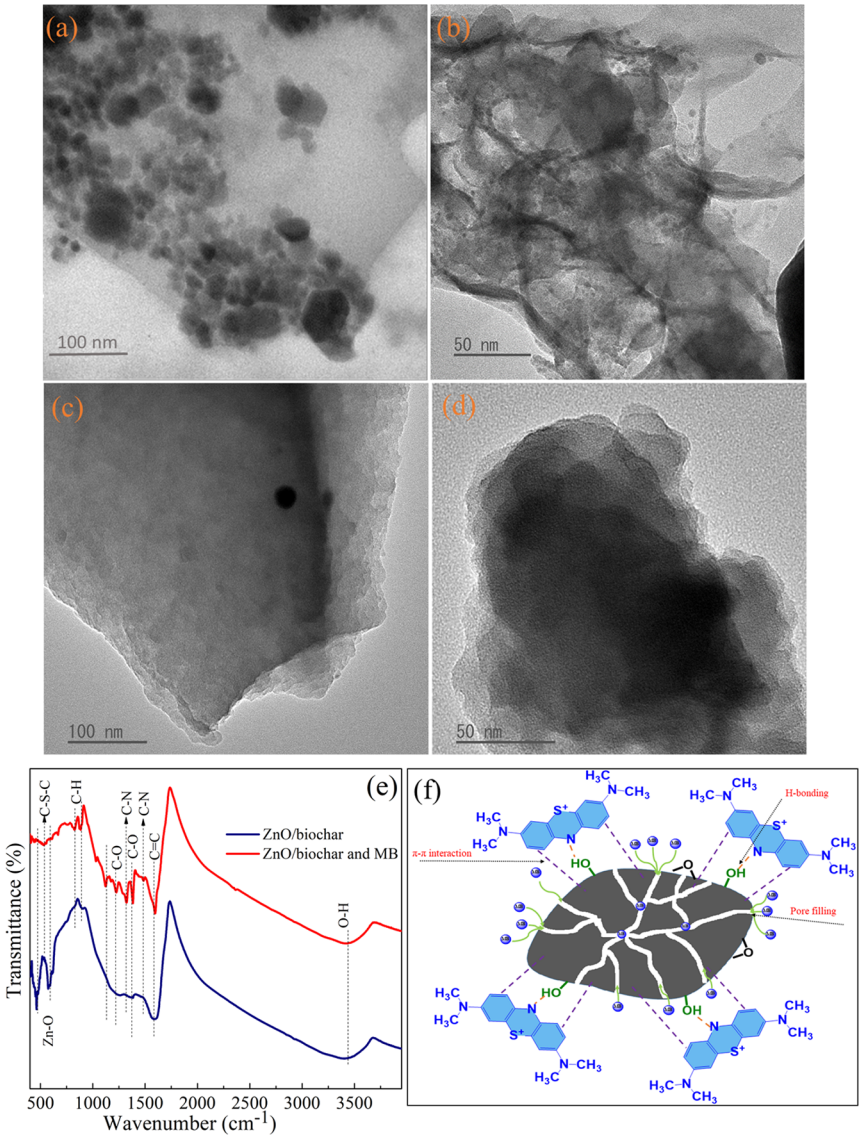

Figure 11. (a,b; c,d) TEM images of the ZnO/biochar before and after MB adsorption, respectively; (e) FTIR spectra; and (f) proposed mechanism for MB adsorption on ZnO/biochar.

istic absorption peaks at 3424 cm^{-1} (−OH) and 1221 cm^{-1} (C−O). In addition, the peaks at 1578 cm^{-1} could be attributed to the stretching vibration of the C═C bond, whereas the peak at 889 cm^{-1} could be due the stretching vibration of the C−H bond. A new absorption peak at 1321 cm^{-1} can be clearly observed in comparison with the FTIR

https://doi.org/10.1021/acsomega.3c01232
ACS Omega 2023, 8, 26816−26827

spectra of ZnO/biochar without MB, and the peak at 1486 cm^{-1} is strengthened in the FTIR spectra of ZnO/biochar after MB adsorption and can be assigned to the vibration of the C−N bond for MB, and the peak at 534 cm^{-1} is assigned to C−S−C of MB (Figure 11e). This indicated that MB was anchored on the surface of ZnO/biochar during the adsorption. The peaks associated with the C═C appear to be narrowed, C−O and C−H for ZnO/biochar showed a significant increase in intensity after MB adsorption. The peak at 3424 cm^{-1} (−OH) remained unchanged but narrowed, most likely due to H-bonding, but because ZnO/biochar contains an OH group, the −NH bond (at 3300−3500 cm^{-1}) is overlapped by the −OH group. Basing on the TEM images and FTIR spectra of ZnO/biochar before and after MB adsorption, we proposed a mechanism for the adsorption of MB on ZnO/biochar materials and the interactions involved using the illustration depicted in Figure 11f. In our experimental adsorption, the pH of the solution was set as 6.1, where the surface of ZnO/biochar is positively charged and MB is a cation dye; the electrostatic repulsion reduced the MB adsorption capacity and efficiency (Figure 8a). Thus, the interaction between the ZnO/biochar material and MB molecules could be mediated primarily by the π-π interaction between the aromatic ring of MB and the π-electron system on the ZnO/biochar surface as well as the H-bonding interaction. Furthermore, the porosity of ZnO/biochar is expected to support the material's adsorption properties because these small pores provide a greater capillary effect and promote better migration of the adsorbate molecule throughout the porous structure of ZnO/biochar.

4. CONCLUSIONS

ZnO/biochar nanocomposites were synthesized by simple one-step pyrolysis under oxygen-limited conditions by using molten $ZnCl_2$ as a chemical activator and precursor of ZnO formation. The porous structure of the as-prepared ZBCs can be tuned by changing the mass ratios of $ZnCl_2$ and the peanut shell precursor and the activation temperature. The BET surface, average pore diameter, and pore volume were 832.1 m^2 g^{-1}, 3.23 nm, and 0.344 cm^3 g^{-1}, respectively. The ZnO/biochar surface has −OH, C−O, C═C, C−H, and Zn−O groups. The XRD, RS, FTIR, SEM, and TEM results demonstrated the existence of ZnO nanoparticles on the biochar surface. Batch experiments were carried out to evaluate the adsorption performance of ZBCs for MB. The results indicated that ZnO/biochar obtained a maximum adsorption capacity of 826.44 mg g^{-1}. The equilibrium study was best fitted with the Langmuir isotherm model. Hence, the ZnO/biochar surface has a high degree of homogeneity and can significantly impart adsorption and chemisorption processes. The proposed adsorption mechanism of the π-π interaction, H-bonding, and pore-filling effect was confirmed. This work provides a basis for developing simple, low-cost, large-scale synthesis of ZBCs for treatment of dyes for various applications.

ASSOCIATED CONTENT

Supporting Information

The Supporting Information is available free of charge at https://pubs.acs.org/doi/10.1021/acsomega.3c01232.

Additional data for MB, MO, and MV adsorption on ZnO/biochar (EDX spectra, fitted model parameters) (PDF)

AUTHOR INFORMATION

Corresponding Author

Dang Van Thanh − *TNU-University of Medicine and Pharmacy, Thai Nguyen, Thainguyen 25000, Vietnam;* orcid.org/0000-0002-8870-6934; Email: thanhdv@tnmc.edu.vn

Authors

Nguyen Thi Luyen − *TNU - University of Sciences, Thai Nguyen, Thainguyen 25000, Vietnam*

Khien Van Nguyen − *TNU - University of Sciences, Thai Nguyen, Thainguyen 25000, Vietnam*

Nguyen Van Dang − *TNU - University of Sciences, Thai Nguyen, Thainguyen 25000, Vietnam*

Tran Quang Huy − *Phenikaa University Nano Institute (PHENA), Phenikaa University, Hanoi 12116, Vietnam; Faculty of Electrical and Electronic Engineering, Phenikaa University, Hanoi 12116, Vietnam*

Pham Hoai Linh − *Institute of Materials Science, Vietnam Academy of Science and Technology, Hanoi 10072, Vietnam*

Nguyen Thanh Trung − *Institute of Physics, Vietnam Academy of Science and Technology, Vietnam Academy of Science and Technology, Hanoi 10072, Vietnam*

Van-Truong Nguyen − *Faculty of Fundamental Sciences, Thai Nguyen University of Technology, Thai Nguyen, Thainguyen 25000, Vietnam*

Complete contact information is available at: https://pubs.acs.org/10.1021/acsomega.3c01232

Author Contributions

N.T.L.: conceptualization, data curation, investigation, methodology, formal analysis, resources, software, visualization, writing-original draw. K.V.N.: formal analysis, methodology. N.V.D., T.Q.H., P.H.L., N.T.T., V.-T.N.: conceptualization, data curation, formal analysis.

Notes

The authors declare no competing financial interest.

ACKNOWLEDGMENTS

This work was financially supported by the Education and Training Ministry of Vietnam (code B2021-TNA-16).

REFERENCES

(1) Kurwadkar, S. Occurrence and Distribution of Organic and Inorganic Pollutants in Groundwater. *Water Environ. Res.* **2019**, *91*, 1001−1008.

(2) Rong, Y.; Li, S.; Niu, J.; Wang, Z.; Hao, X.; Song, C.; Wang, T.; Guan, G. Carbon-Based Electroactive Ion Exchange Materials: Ultrahigh Removal Efficiency and Ion Selectivity for Rapid Removal of Cs^+ Ions. *Sep. Purif. Technol.* **2021**, *274*, No. 119056.

(3) Qiu, B.; Tao, X.; Wang, H.; Li, W.; Ding, X.; Chu, H. Biochar as a Low-Cost Adsorbent for Aqueous Heavy Metal Removal: A Review. *J. Anal. Appl. Pyrolysis* **2021**, *155*, No. 105081.

(4) Dai, Y.; Zhang, N.; Xing, C.; Cui, Q.; Sun, Q. The Adsorption, Regeneration and Engineering Applications of Biochar for Removal Organic Pollutants: A Review. *Chemosphere* **2019**, *223*, 12−27.

(5) Gwenzi, W.; Chaukura, N.; Wenga, T.; Mtisi, M. Biochars as Media for Air Pollution Control Systems: Contaminant Removal Applications and Future Research Directions. *Sci. Total Environ.* **2021**, *753*, No. 142249.

(6) Yu, Q.; Zou, J.; Peng, G.; Gao, F.; Gao, Y.; Guorong Fan, S. C.; Lu, L. A Facile Fabrication of Ratiometric Electrochemical Sensor for Sensitive Detection of Riboflavin Based on Hierarchical Porous

Biochar Derived from KOH-Activated Soulangeana Sepals. *Nanotechnology* **2022**, *33*, 445501.
(7) Zhu, Y.; Yi, B.; Yuan, Q.; Wu, Y.; Wang, M.; Yan, S. Removal of Methylene Blue from Aqueous Solution by Cattle Manure-Derived Low Temperature Biochar. *RSC Adv.* **2018**, *8*, 19917−19929.
(8) Egbedina, A. O.; Adebowale, K. O.; Olu-Owolabi, B. I.; Unuabonah, E. I.; Adesina, M. O. Green Synthesis of ZnO Coated Hybrid Biochar for the Synchronous Removal of Ciprofloxacin and Tetracycline in Wastewater. *RSC Adv.* **2021**, *11*, 18483−18492.
(9) Rashid, R.; Shafiq, I.; Akhter, P.; Iqbal, M. J.; Hussain, M. A State-of-the-Art Review on Wastewater Treatment Techniques: The Effectiveness of Adsorption Method. *Environ. Sci. Pollut. Res.* **2021**, *28*, 9050−9066.
(10) Zhao, C.; Wang, B.; Theng, B. K. G.; Wu, P.; Liu, F.; Wang, S.; Lee, X.; Chen, M.; Li, L.; Zhang, X. Formation and Mechanisms of Nano-Metal Oxide-Biochar Composites for Pollutants Removal: A Review. *Sci. Total Environ.* **2021**, *767*, No. 145305.
(11) Chausali, N.; Saxena, J.; Prasad, R. Nanobiochar and Biochar Based Nanocomposites: Advances and Applications. *J. Agric. Food Res.* **2021**, *5*, No. 100191.
(12) Van, H. T.; Nguyen, L. H.; Dang, N. V.; Chao, H. P.; Nguyen, Q. T.; Nguyen, T. H.; Nguyen, T. B. L.; Van Thanh, D.; Nguyen, H. D.; Thang, P. Q.; Thanh, P. T. H.; Hoang, V. P. The Enhancement of Reactive Red 24 Adsorption from Aqueous Solution Using Agricultural Waste-Derived Biochar Modified with ZnO Nanoparticles. *RSC Adv.* **2021**, *11*, 5801−5814.
(13) Weidner, E.; Karbassiyazdi, E.; Altaee, A.; Jesionowski, T.; Ciesielczyk, F. Hybrid Metal Oxide/Biochar Materials for Wastewater Treatment Technology: A Review. *ACS Omega* **2022**, *7*, 27062−27078.
(14) Mankomal, H.; Kaur, H. Synergistic Effect of Biochar Impregnated with ZnO Nano-Flowers for Effective Removal of Organic Pollutants from Wastewater. *Appl. Surf. Sci. Adv* **2022**, *12*, No. 100339.
(15) Akpomie, K. G.; Conradie, J. Synthesis, Characterization, and Regeneration of an Inorganic−Organic Nanocomposite (ZnO@biomass) and Its Application in the Capture of Cationic Dye. *Sci. Rep.* **2020**, *10*, 1−12.
(16) Yang, B.; Zhang, M.; Wu, M.; Zhang, H.; Song, Q.; Yu, S. Synthesis of Biochar-Based Cu_2O Nanoparticles and Their Antibacterial Activity against Escherichia Coli. *Inorg. Nano-Metal Chem.* **2019**, *49*, 12−16.
(17) Chen, M.; Bao, C.; Hu, D.; Jin, X.; Huang, Q. Facile and Low-Cost Fabrication of ZnO/Biochar Nanocomposites from Jute Fibers for Efficient and Stable Photodegradation of Methylene Blue Dye. *J. Anal. Appl. Pyrolysis* **2019**, *139*, 319−332.
(18) Lou, J.; Xu, X.; Gao, Y.; Zheng, D.; Wang, J.; Li, Z. Preparation of Magnetic Activated Carbon from Waste Rice Husk for the Determination of Tetracycline Antibiotics in Water Samples. *RSC Adv.* **2016**, *6*, 112166−112174.
(19) Gonçalves, M. G.; da Silva Veiga, P. A.; Fornari, M. R.; Peralta-Zamora, P.; Mangrich, A. S.; Silvestri, S. Relationship of the Physicochemical Properties of Novel ZnO/Biochar Composites to Their Efficiencies in the Degradation of Sulfamethoxazole and Methyl Orange. *Sci. Total Environ.* **2020**, *748*, No. 141381.
(20) Alhan, S.; Nehra, M.; Dilbaghi, N.; Singhal, N. K.; Kim, K. H.; Kumar, S. Potential Use of ZnO@activated Carbon Nanocomposites for the Adsorptive Removal of Cd^{2+} Ions in Aqueous Solutions. *Environ. Res.* **2019**, *173*, 411−418.
(21) Wang, S.; Zhou, Y.; Han, S.; Wang, N.; Yin, W.; Yin, X.; Gao, B.; Wang, X.; Wang, J. Carboxymethyl Cellulose Stabilized ZnO/Biochar Nanocomposites: Enhanced Adsorption and Inhibited Photocatalytic Degradation of Methylene Blue. *Chemosphere* **2018**, *197*, 20−25.
(22) Shang, H.; Lu, Y.; Zhao, F.; Chao, C.; Zhang, B.; Zhang, H. Preparing High Surface Area Porous Carbon from Biomass by Carbonization in a Molten Salt Medium. *RSC Adv.* **2015**, *5*, 75728−75734.
(23) Xia, D.; Tan, F.; Zhang, C.; Jiang, X.; Chen, Z.; Li, H.; Zheng, Y.; Li, Q.; Wang, Y. $ZnCl_2$ -Activated Biochar from Biogas Residue Facilitates Aqueous As(III) Removal. *Appl. Surf. Sci.* **2016**, *377*, 361−369.
(24) Bassey, E.; Yang, L.; Cao, M.; Feng, Y.; Yao, J. Molten Salt Synthesis of Capacitive Porous Carbon from Allium Cepa (Onion) for Supercapacitor Application. *J. Electroanal. Chem.* **2021**, *881*, No. 114972.
(25) Ahmed, M. B.; Zhou, J. L.; Ngo, H. H.; Guo, W.; Chen, M. Progress in the Preparation and Application of Modified Biochar for Improved Contaminant Removal from Water and Wastewater. *Bioresour. Technol.* **2016**, *214*, 836−851.
(26) Wang, L.; Zhou, P.; Guo, Y.; Zhang, J.; Qiu, X.; Guan, Y.; Yu, M.; Zhu, H.; Zhang, Q. The Effect of $ZnCl_2$ Activation on Microwave Absorbing Performance in Walnut Shell-Derived Nano-Porous Carbon. *RSC Adv.* **2019**, *9*, 9718−9728.
(27) Dos Reis, G. S.; Wilhelm, M.; Silva, T. C. D. A.; Rezwan, K.; Sampaio, C. H.; Lima, E. C.; De Souza, S. M. A. G. U. The Use of Design of Experiments for the Evaluation of the Production of Surface Rich Activated Carbon from Sewage Sludge via Microwave and Conventional Pyrolysis. *Appl. Therm. Eng.* **2016**, *93*, 590−597.
(28) Wang, X.; Liang, X.; Wang, Y.; Wang, X.; Liu, M.; Yin, D.; Xia, S.; Zhao, J.; Zhang, Y. Adsorption of Copper (II) onto Activated Carbons from Sewage Sludge by Microwave-Induced Phosphoric Acid and Zinc Chloride Activation. *Desalination* **2011**, *278*, 231−237.
(29) Wang, Y.; Wang, L.; Deng, X.; Gao, H. A Facile Pyrolysis Synthesis of Biochar/ZnO Passivator: Immobilization Behavior and Mechanisms for Cu (II) in Soil. *Environ. Sci. Pollut. Res.* **2020**, *27*, 1888−1897.
(30) Lourenco, M. A. O.; Zeng, J.; Jagdale, P.; Castellino, M.; Sacco, A.; Farkhondehfal, M. A.; Pirri, C. F. Biochar/Zinc Oxide Composites as Effective Catalysts for Electrochemical CO_2 Reduction. *ACS Sustainable Chem. Eng.* **2021**, *9*, 5445−5453.
(31) Yu, F.; Tian, F.; Zou, H.; Ye, Z.; Peng, C.; Huang, J.; Zheng, Y.; Zhang, Y.; Yang, Y.; Wei, X.; Gao, B. ZnO/Biochar Nanocomposites via Solvent Free Ball Milling for Enhanced Adsorption and Photocatalytic Degradation of Methylene Blue. *J. Hazard. Mater.* **2021**, *415*, No. 125511.
(32) Pawlyta, M.; Rouzaud, J. N.; Duber, S. Raman Microspectroscopy Characterization of Carbon Blacks: Spectral Analysis and Structural Information. *Carbon N. Y.* **2015**, *84*, 479−490.
(33) Franklin, R. E. The Structure of Graphitic Carbons. *Acta Crystallogr.* **1951**, *4*, 253−261.
(34) Chen, L.; Hu, J.; Han, Q.; Zhang, J.; Zhou, Z.; Zhou, N.; Zhou, H.; Lu, X.; Mi, B.; Wu, F. Resolving the Enhancement Effect of Microwave-Assisted Pyrolysis on Biochar Redox Properties from the Structure-Activity Relationship. *J. Anal. Appl. Pyrolysis* **2022**, *167*, No. 105706.
(35) Snedeker, L. P.; Risbud, A. S.; Masala, O.; Zhang, J. P.; Seshadri, R. Organic Phase Conversion of Bulk (Wurtzite) ZnO to Nanophase (Wurtzite and Zinc Blende) ZnO. *Solid State Sci.* **2005**, *7*, 1500−1505.
(36) Zhang, F.; Liu, L.; Chen, L.; Shi, Y. A Cellulose Dissolution and Encapsulation Strategy to Prepare Carbon Nanospheres with Ultra-Small Size and High Nitrogen Content for the Oxygen Reduction Reaction. *New J. Chem.* **2020**, *44*, 10613−10620.
(37) Fu, L. H.; Dong, Y. Y.; Ma, M. G.; Li, S. M.; Sun, S. L.; Sun, R. C. $Zn_5(OH)_8Cl_2{\cdot}H_2O$ Sheets Formed Using Cellulose as Matrix via Microwave-Assisted Method and Its Transformation to ZnO. *Mater. Lett.* **2013**, *92*, 136−138.
(38) Li, Y.; Shang, T. X.; Gao, J. M.; Jin, X. J. Nitrogen-Doped Activated Carbon/Graphene Composites as High-Performance Supercapacitor Electrodes. *RSC Adv.* **2017**, *7*, 19098−19105.
(39) Guo, W.; Zhao, B.; Zhou, Q.; He, Y.; Wang, Z.; Radacsi, N. Fe-Doped ZnO/Reduced Graphene Oxide Nanocomposite with Synergic Enhanced Gas Sensing Performance for the Effective Detection of Formaldehyde. *ACS Omega* **2019**, *4*, 10252−10262.
(40) Madhu, R.; Veeramani, V.; Chen, S. M.; Veerakumar, P.; Liu, S.; Miyamoto, N. Functional Porous Carbon-ZnO Nanocomposites

https://doi.org/10.1021/acsomega.3c01232
ACS Omega 2023, 8, 26816−26827

for High-Performance Biosensors and Energy Storage Applications. *Phys. Chem. Chem. Phys.* **2016**, *18*, 16466−16475.
(41) Gonçalves, N. P. F.; Lourenço, M. A. O.; Baleuri, S. R.; Bianco, S.; Jagdale, P.; Calza, P. Biochar Waste-Based ZnO Materials as Highly Efficient Photocatalysts for Water Treatment. *J. Environ. Chem. Eng.* **2022**, *10*, No. 107256.
(42) Jing, H.; Ji, L.; Wang, Z.; Guo, J.; Lu, S.; Sun, J.; Lu, C. Synthesis of ZnO Nanoparticles Loaded on Biochar Derived from Spartina Alterniflora with Superior Photocatalytic Degradation Performance. *Nanomaterials* **2021**, *11*, 2479.
(43) Rodríguez-Sánchez, S.; Ruiz, B.; Martínez-Blanco, D.; Sánchez-Arenillas, M.; Diez, M. A.; Suárez-Ruiz, I.; Marco, J. F.; Blanco, J.; Fuente, E. Sustainable Thermochemical Single-Step Process to Obtain Magnetic Activated Carbons from Chestnut Industrial Wastes. *ACS Sustainable Chem. Eng.* **2019**, *7*, 17293−17305.
(44) Georgin, J.; Dotto, G. L.; Mazutti, M. A.; Foletto, E. L. Preparation of Activated Carbon from Peanut Shell by Conventional Pyrolysis and Microwave Irradiation-Pyrolysis to Remove Organic Dyes from Aqueous Solutions. *J. Environ. Chem. Eng.* **2016**, *4*, 266−275.
(45) Dobrucka, R.; Długaszewska, J. Biosynthesis and Antibacterial Activity of ZnO Nanoparticles Using Trifolium Pratense Flower Extract. *Saudi J. Biol. Sci.* **2016**, *23*, 517−523.
(46) Arami-Niya, A.; Daud, W. M. A. W.; Mjalli, F. S. Using Granular Activated Carbon Prepared from Oil Palm Shell by $ZnCl_2$ and Physical Activation for Methane Adsorption. *J. Anal. Appl. Pyrolysis* **2010**, *89*, 197−203.
(47) Guo, S.; Peng, J.; Li, W.; Yang, K.; Zhang, L.; Zhang, S.; Xia, H. Effects of CO_2 Activation on Porous Structures of Coconut Shell-Based Activated Carbons. *Appl. Surf. Sci.* **2009**, *255*, 8443−8449.
(48) Chen, C.; Mi, S.; Lao, D.; Shi, P.; Tong, Z.; Li, Z.; Hu, H. Single-Step Synthesis of Eucalyptus Sawdust Magnetic Activated Carbon and Its Adsorption Behavior for Methylene Blue. *RSC Adv.* **2019**, *9*, 22248−22262.
(49) Díez, N.; Fuertes, A. B.; Sevilla, M. Molten Salt Strategies towards Carbon Materials for Energy Storage and Conversion. *Energy Storage Mater.* **2021**, *38*, 50−69.
(50) Jones, F.; Tran, H.; Lindberg, D.; Zhao, L.; Hupa, M. Thermal Stability of Zinc Compounds. *Energy Fuels* **2013**, *27*, 5663−5669.
(51) Ji, Y.; Xu, F.; Wei, W.; Gao, H.; Zhang, K.; Zhang, G.; Xu, Y.; Zhang, P. Efficient and Fast Adsorption of Methylene Blue Dye onto a Nanosheet MFI Zeolite. *J. Solid State Chem.* **2021**, *295*, No. 121917.
(52) Cordova Estrada, A. K.; Cordova Lozano, F.; Lara Díaz, R. A. Thermodynamics and Kinetic Studies for the Adsorption Process of Methyl Orange by Magnetic Activated Carbons. *Air, Soil Water Res.* **2021**, *14*, No. 117862212110133.
(53) Rai, P.; Gautam, R. K.; Banerjee, S.; Rawat, V.; Chattopadhyaya, M. C. Synthesis and Characterization of a Novel $SnFe_2O_4$@activated Carbon Magnetic Nanocomposite and Its Effectiveness in the Removal of Crystal Violet from Aqueous Solution. *J. Environ. Chem. Eng.* **2015**, *3*, 2281−2291.
(54) Kamdod, A. S.; Kumar, M. V. P. Adsorption of Methylene Blue, Methyl Orange, and Crystal Violet on Microporous Coconut Shell Activated Carbon and Its Composite with Chitosan: Isotherms and Kinetics. *J. Polym. Environ.* **2022**, *30*, 5274−5289.
(55) Li, Y.; Du, Q.; Liu, T.; Peng, X.; Wang, J.; Sun, J.; Wang, Y.; Wu, S.; Wang, Z.; Xia, Y.; Xia, L. Comparative Study of Methylene Blue Dye Adsorption onto Activated Carbon, Graphene Oxide, and Carbon Nanotubes. *Chem. Eng. Res. Des.* **2013**, *91*, 361−368.
(56) Bu, J.; Yuan, L.; Zhang, N.; Meng, Y.; Peng, X. Novel Adsorbent of N-Phenylthiourea-Functionalized Graphene Oxide and Its Removal of Methyl Orange in Aqueous Solutions. *J. Chem. Eng. Data* **2021**, *66*, 199−209.
(57) Ramesha, G. K.; Vijaya Kumara, A.; Muralidhara, H. B.; Sampath, S. Graphene and Graphene Oxide as Effective Adsorbents toward Anionic and Cationic Dyes. *J. Colloid Interface Sci.* **2011**, *361*, 270−277.
(58) Ma, J.; Yu, F.; Zhou, L.; Jin, L.; Yang, M.; Luan, J.; Tang, Y.; Fan, H.; Yuan, Z.; Chen, J. Enhanced Adsorptive Removal of Methyl Orange and Methylene Blue from Aqueous Solution by Alkali-Activated Multiwalled Carbon Nanotubes. *ACS Appl. Mater. Interfaces* **2012**, *4*, 5749−5760.
(59) Sabna, V.; Thampi, S. G.; Chandrakaran, S. Adsorption of Crystal Violet onto Functionalised Multi-Walled Carbon Nanotubes: Equilibrium and Kinetic Studies. *Ecotoxicol. Environ. Saf.* **2016**, *134*, 390−397.
(60) Radoor, S.; Karayil, J.; Jayakumar, A.; Parameswaranpillai, J.; Siengchin, S. Efficient Removal of Methyl Orange from Aqueous Solution Using Mesoporous ZSM-5 Zeolite: Synthesis, Kinetics and Isotherm Studies. *Colloids Surfaces A Physicochem. Eng. Asp* **2021**, *611*, No. 125852.
(61) Brião, G. V.; Jahn, S. L.; Foletto, E. L.; Dotto, G. L. Adsorption of Crystal Violet Dye onto a Mesoporous ZSM-5 Zeolite Synthetized Using Chitin as Template. *J. Colloid Interface Sci.* **2017**, *508*, 313−322.
(62) Meili, L.; Lins, P. V.; Zanta, C. L. P. S.; Soletti, J. I.; Ribeiro, L. M. O.; Dornelas, C. B.; Silva, T. L.; Vieira, M. G. A. MgAl-LDH/Biochar Composites for Methylene Blue Removal by Adsorption. *Appl. Clay Sci.* **2019**, *168*, 11−20.
(63) Kim, J.; Bak, G.-H.; Yoo, D.-Y.; Lee, Y.-I.; Lee, Y.-G.; Chon, K. Functionalization of Pine Sawdust Biochars with Mg/Al Layered Double Hydroxides to Enhance Adsorption Capacity of Synthetic Azo Dyes: Adsorption Mechanisms and Reusability. *Heliyon* **2023**, *9*, No. e14142.
(64) Tan, X.; Liu, Y. G.; Gu, Y. L.; Liu, S. B.; Zeng, G. M.; Cai, X.; Hu, X. J.; Wang, H.; Liu, S. M.; Jiang, L. H. Biochar Pyrolyzed from MgAl-Layered Double Hydroxides Pre-Coated Ramie Biomass (Boehmeria Nivea (L.) Gaud.): Characterization and Application for Crystal Violet Removal. *J. Environ. Manage.* **2016**, *184*, 85−93.

https://doi.org/10.1021/acsomega.3c01232
ACS Omega 2023, 8, 26816−26827